TITLE

Topographic Correction of Visible Near-Infrared Reflectance Spectra for Horizon-Scale Soil Organic Carbon Mapping

Abbreviations

HSI, laboratory-based hyperspectral imaging; KGE, Kling-Gupta Efficiency; MLR, multiple linear regression; MLT, multistripe laser triangulation; NSE, Nash-Sutcliffe Efficiency; PLSR, partial least squares regression; RI, reflectance intensity; RRI, reference reflectance intensity; URI, uncorrected reflectance intensity; SOC, soil organic carbon; SOC_o, observed SOC; SOC_p, predicted SOC; VNIR, visible near-infrared; ϕ_o, aspect angle; η, slope angle; ϕ_a, azimuth angle; λ, waveband.

Core Ideas

- A novel topographic correction method reduced the effect of surface orientation on lab-based soil reflectance.
- A linear empirical approach outperformed two versions of a geometric topographic correction.
- Bias and error in SOC predictions were decreased when topographically-corrected reflectance spectra were used.
- Topographic correction advances the use of HSI on intact soil samples displaying natural roughness.

ABSTRACT

Understanding soil organic carbon (SOC) response to global change has been hindered by an inability to map SOC at horizon scales relevant to coupled hydrologic and biogeochemical processes. Standard SOC measurements rely on homogenized samples taken from distinct depth intervals. Such sampling prevents an examination of fine-scale SOC distribution within a soil horizon. Visible near-infrared hyperspectral imaging (HSI) has been applied to intact monoliths and split cores surfaces to overcome this limitation. However, the roughness of these surfaces can influence HSI spectra by scattering reflected light in different directions posing challenges to fine-scale SOC mapping. Here we examine the influence of prescribed surface orientation on reflected spectra, develop a method for correcting topographic effects, and calibrate a partial least squares regression (PLSR) model for SOC prediction. Two empirical models that account for surface slope, aspect, and wavelength and two theoretical models that account for the geometry of the spectrometer were compared using 681 homogenized soil samples from across the US that were packed into sample wells and presented to the spectrometer at 91 orientations. The empirical approach outperformed the more complex geometric models in

This article has been accepted for publication and undergone full peer review but has not been through the copyediting, typesetting, pagination and proofreading process, which may lead to differences between this version and the Version of Record. Please cite this article as doi: 10.1002/saj2.20612.

correcting spectra taken at non-flat configurations. Topographically-corrected spectra reduced bias and error in SOC predicted by PLSR, particularly at slope angles greater than 30°. Our approach clears the way for investigating the spatial distributions of multiple soil properties on rough intact soil samples.

1 INTRODUCTION

The spatial arrangement of soil material and concomitant void space is a key determinant of water, energy, and gas fluxes within the critical zone (Sullivan et al., 2022). Despite its importance, few studies characterize the spatial arrangements of soil solid constituents at the scales necessary to understand many of the hydrologic and biogeochemical processes controlling these fluxes. In particular, the type, location, and abundance of soil organic carbon (SOC) controls water and nutrient cycling and biological activity within soils (Lal, 2004; Banwart, 2014; Wiesmeier et al., 2019) and development of soil structure (Bronick et al., 2005; Or et al., 2021)—a physical property of soils which describes the size, shape, and spatial arrangement of soil aggregates and pore networks (Letey, 1991). Despite decades of research on SOC storage (Six et al., 2004; Basile-Doelsch et al., 2020), advancements in our understanding of how and where SOC is stored within soils are needed (Davidson & Janssens, 2006; McBratney et al., 2014; Lehmann & Kleber, 2015) and it is expected that a better understanding of the mechanistic relationships between SOC storage and soil structure would support these advancements (Stockmann, 2013).

Studies of the relationships between SOC storage and soil structure are, however, limited by a lack of sufficient observations that quantify the fine-scale spatial distribution of SOC (Rabot et al., 2018). One reason for this limitation is that standard methods for SOC quantification rely on homogenized bulk soil material sampled from particular depth intervals (e.g., within a described morphological horizon) and, thus, fail to characterize fine-scale spatial variability that would be retained in intact samples. Advancing our ability to study soil properties on intact samples that retain the natural soil architecture is key to understanding and modeling soil behavior and predicting future changes in soil function (Lucas et al., 2020; Vogel et al., 2021).

Driven by the need for methods capable of non-destructively studying intact soil samples, proximal sensing approaches have been developed that open the door to high-resolution, spatially-explicit characterization of soil constituents and soil structure at scales relevant to soil hydrologic processes like preferential flow (e.g., horizon to pedon scales) (Hirmas, 2016). One of these methods, visible near-infrared (VNIR) hyperspectral imaging (HSI) spectroscopy, offers a promising way forward in quantifying the horizon-scale spatial distribution of soil chemical properties (Buddenbaum & Steffens, 2012a, 2012b; Steffens & Buddenbaum, 2013; Steffens et al., 2014; Hobley et al., 2018; Steffens et al. 2021). Hyperspectral imaging collects reflectance spectra from a soil surface at high spatial resolution (e.g., sub-millimeter) without disrupting the arrangement of constituents. These spectral signatures are used to calibrate empirical regression models to predict soil properties for each pixel on the soil surface of an intact sample, thereby mapping the spatial distribution of soil properties.

However, VNIR reflectance spectra are sensitive to surface topography (Baumgardner, 1985; Civco, 1989) resulting in inconsistencies in soil spectral data and decreases in the reliability of predictions made from spectra collected at different surface orientations (Ben Dor et.al, 2015). Previous studies utilizing HSI have reduced the impact of surface roughness on the spectral signatures by slicing the surface of intact soil monoliths or splitting cores flat before imaging (Hobley et al., 2018; Steffens et al., 2014; Steffens & Buddenbaum, 2013). Unfortunately, surface flattening restricts the application of other proximal sensing methods on these samples such as multistripe laser triangulation (MLT) used to characterize macropore networks and soil structure (Eck et al., 2013; Hirmas et al., 2016; Bagnall et al., 2020). Therefore, simultaneous investigation of the spatial distribution of solid constituents like SOC and structure using a combination of HSI and MLT scanning is not yet possible. While methods exist to prepare intact soil surfaces to preserve the natural structure for MLT analysis (Hirmas, 2013), the development of a post-imaging topographic-correction method for laboratory-based proximal sensing techniques like HSI is lacking. Therefore, a topographic correction would have the advantage of allowing HSI to be applied to intact samples that have been prepared for characterization of soil structure and macroporosity.

In remote sensing applications, two geometric topographic correction methods—the cosine correction and C-correction (Teillet et al., 1982)—have been developed to correct reflectance spectra for the influence of surface orientation (Hantson & Chuvieco, 2011). However, it is unclear how well these corrections perform in lab-based proximal sensing applications or how to translate these methods into a laboratory setting since several of their parameters, such as aspect and azimuth angles, must be defined differently in the laboratory than for remote sensing applications. In this study, we aimed to evaluate the effect of surface slope and aspect on VNIR reflectance spectra measured by HSI using homogenized soil samples presented at prescribed surface orientations, compare several empirical regression and geometric approaches to correct this effect, and calibrate a model to predict SOC from corrected spectra. Although the parameters of the empirical correction model developed here are likely specific to the HSI spectrometer used in this work (e.g., due to differences in setup geometries), our overall goal was to develop a procedural framework by which VNIR spectra measured by HSI can be topographically corrected for other similar instruments to enable the tandem spatial analysis of SOC and soil structure from the surfaces of intact soil samples.

2 MATERIALS AND METHODS

2.1 Sample Locations and Characterization

A total of 681 ground soil samples taken from three soil sample archives were included from a variety of locations across the conterminous USA to ensure that a wide range of soil properties such as soil color, texture, and SOC were represented (Table 1; Figure 1). This was done to allow future application of calibration equations to soil samples from a variety of locations and environments.

The first group consisted of 574 samples and was provided by the NEON Initial Characterization Soils Archive at the University of Michigan Biological Station-Sample Archive Facility in Ehlers (UMBS-SAFE). The accompanying soil properties data were obtained from the NEON Data Archive. These samples were collected from 150 distributed pits across 6 core and 4 gradient terrestrial field sites spanning 7 ecoclimatic domains within NEON (Figure 1; Table S1). The NEON soil samples were dried, ground, and sieved; particle-size distribution was determined using the pipette method and weight percent carbon was determined by elemental analysis using a CN analyzer (Browning & Stanish, 2017; Schoeneberger et al., 2012; Soil Survey Staff, 2022).

A second group of 50 soil samples was collected from Duke Farms in Hillsborough Township, New Jersey (Figure 1). The Duke Farms soil samples were dried, ground, and sieved, and weight percent carbon was determined by elemental analysis using a CN analyzer (Vario MAX Cub, Elementar Americas, Inc., Ronkonkoma, NY).

A third group of 57 soil samples was collected in 2018 and 2019 from locations in the Santa Ana Mountains of California that were affected by the 2018 Holy Fire to include soils with pyrogenic carbon (Figure 1). The Holy Fire soil samples were dried, ground, and sieved, and weight percent carbon was determined by elemental analysis using a CN analyzer (Flash EA, Thermo Fisher Scientific, Waltham, MA).

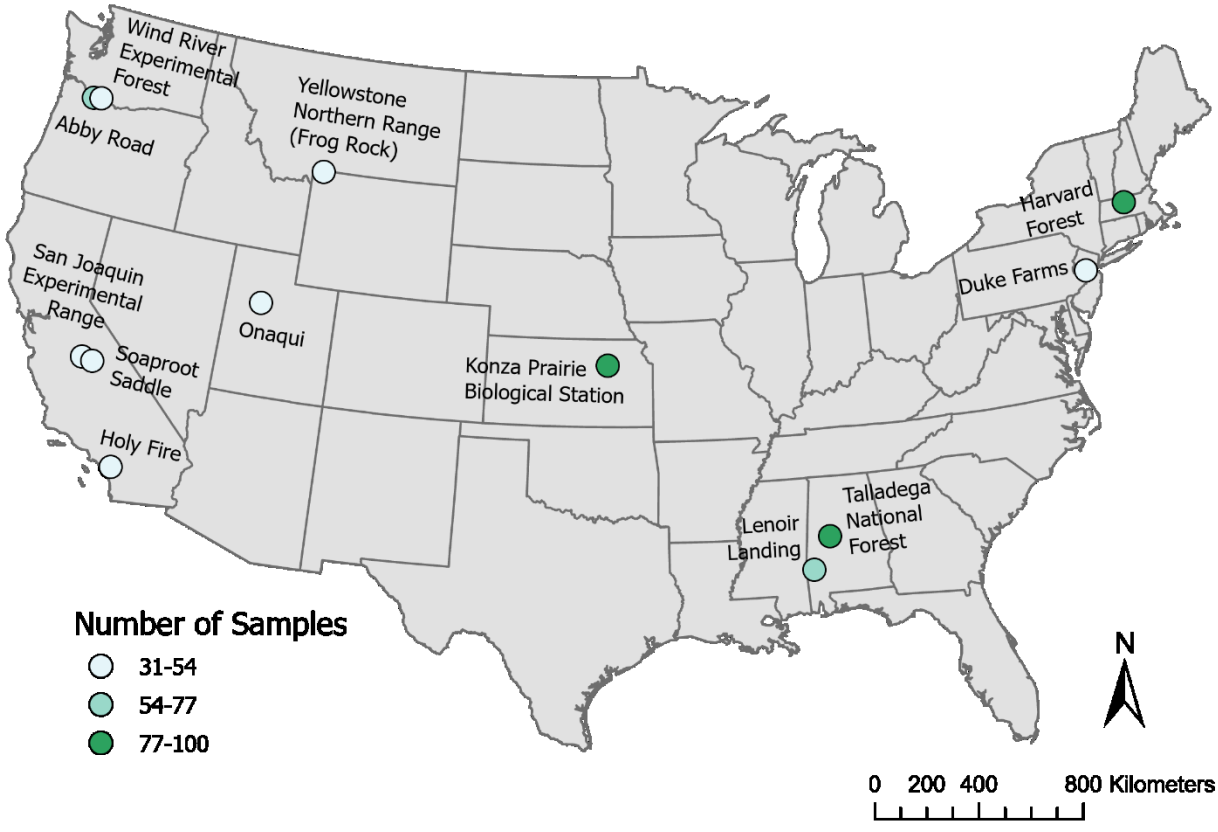

FIGURE 1: Circles show locations of sampling sites for soil samples used this study. Circle color indicates the number of soil samples obtained from each site (also see Table S2).

2.2 Sample Preparation for HSI Scanning

Soil samples were packed into custom-designed rectangular sample wells (Figure 2) with an inner volume of 0.4 cm^3 for HSI scanning. The mass of these wells was recorded before and after packing and used to calculate the packed bulk density. We packed soil samples into sample wells to achieve bulk density values that are representative of in situ soils. Gravimetric air-dried soil moisture was determined on a separate aliquot of each sample to correct the packed bulk density to a dry-soil basis. We converted SOC from a mass basis to a volumetric basis using the packed bulk density because reflectance spectra represent an area rather than a mass.

Care was taken to uniformly pack and flatten the surfaces of soil samples using a stainless-steel micro spatula to eliminate depressions, cracks, or peaks. This procedure ensured that any differences in reflectance spectra obtained at different surface orientations was attributable to the prescribed surface geometry of the sampling array and not to differences in sample preparation (e.g., shadowing due to micro-topography within sample wells).

2.3 Sample Well Array

A web-based three-dimensional (3-D) modeling application (SketchUp Free Ver. 1.3, Trimble, Westminster, CO) was used to design all components of the sample well array (Figure 2). Sample wells were designed to hold approximately 0.5 g of soil and rectangular prism-shaped tampers were designed to evenly pack soil samples into the sample wells. Sample trays were designed to hold 20 sample wells in place at prescribed slope and aspect positions. We designed 6 triangular prisms to hold a tray on each sloped face at 10°, 20°, 30°, 40°, 50°, or 60° slope angle. A separate base tray was designed to fit two triangular prisms so that 40 soil samples could be scanned at the same time (i.e., one sample tray per triangular prism with both sample trays placed on the same side of each prism) (Figures 2 and 3).

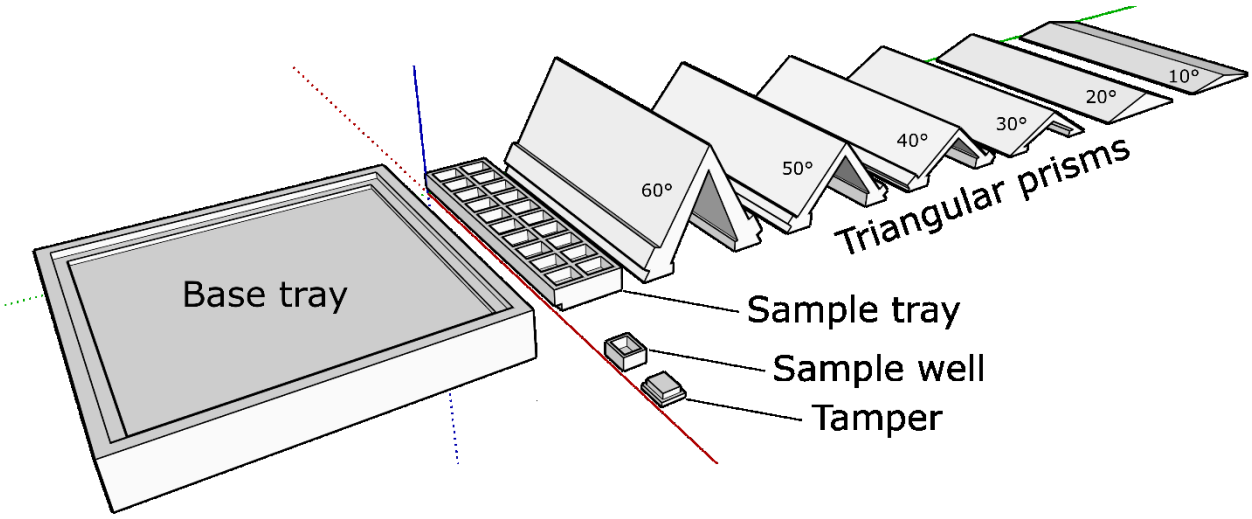

FIGURE 2: Custom-designed and 3-D printed sample well array used in this study to present soil samples at 7 slope orientations under the hyperspectral camera. Aspects were imposed by rotating the base tray while keeping it centered under the hyperspectral camera (Figure 3).

All components of the sample well array were fabricated using a 3-D printer (Form 3, Formlabs Inc., Somerville, MA). We used a heat resistant resin (High Temp Resin V2, Formlabs Inc., Somerville, MA) with a heat deflection temperature of 238°C to ensure the integrity of the sample array under the focused heat emitted by the halogen lamp light sources during HSI scanning. Following initial fabrication, each part was washed (Form Wash, Formlabs, Inc., Somerville, MA) in an agitated solution of isopropyl alcohol for 6 min and cured (Form Cure, Formlabs, Inc., Somerville, MA) using a 405 nm wavelength light source at 80°C for 120 min.

2.4 HSI Scanning Setup

Hyperspectral imaging was performed with a high-sensitivity sCMOS VNIR hyperspectral camera (MSV 500, Middleton Spectral Vision, Middleton, WI) which collects reflectance intensities (RI) at 471 wavebands between 400-1000 nm at a spectral and spatial resolution of 1.2 nm and 250 µm, respectively (Figure 3A). A motorized scanning stage (ViaSpec Geo II, Middleton Spectral Vision, Middleton, WI) was used in conjunction with data acquisition software (FastFrame, Middleton Spectral Vision, Middleton, WI) to control the lateral positioning of the camera relative to the samples as well as the push-broom motion of the scan stage (Figure 3A). Samples were scanned at a frame rate of 29.967 Hz with an integration time of 7.641 ms and scan speed of 0.706 cm s^{-1}. Scans were collected in the dark in a windowless laboratory space such that the only sources of light were two light banks each consisting of 8 halogen light bulbs with front glass covers (Reflekto MR-11 12V 35W 36° Flood, Ushio America, Inc., Cypress, CA,).

Aspect was taken as the angle that the surface of the soil sample was facing in relation to the forward motion of the scan stage. Thus, aspects were assigned 0°N when they faced the

direction of movement of the scan stage under the hyperspectral camera (i.e., from light bank 2 toward light bank 1) (Figure 4). Aspect angles (ϕ_o) were prescribed in degrees clockwise from the 0° N reference by rotating the center of the base tray prior to scanning (Figure 3B). Initially, RI at 14 aspects (0°, 15°, 30°, 45°, 60°, 75°, 90°, 180°, 195°, 210°, 225°, 240°, 255°, and 270°) were collected. However, spectra collected at aspects of 195°, 210°, 225°, 240°, 255°, and 270° were converted to 165°, 150°, 135°, 120°, 105°, and 90°, respectively, during post-processing so that the ϕ_o values varied only between 0° and 180°. The intensities of each wavelength for the initial 90° aspect and the 90° aspect converted from 270° were averaged to yield a single 90° spectra. Thus, we analyzed sample spectra collected at 13 different aspects for each slope orientation.

Slope angle (η) is defined as the angle between the surface of the soil sample being scanned and the scan stage such that a soil surface within a sample well at a 0° slope is parallel to the scan stage but perpendicular to the orientation of the hyperspectral camera (Figure 4). Spectra were obtained at 7 slope angles (i.e., 0°, 10°, 20°, 30°, 40°, 50°, and 60°) at each aspect. Zero slope angles were achieved by arranging the sample trays directly on the base tray, while non-zero slopes were imposed using identical pairs of each of the 6 fabricated triangular prisms (Figure 2-4). These slope and aspect configurations resulted in 91 scans per soil sample.

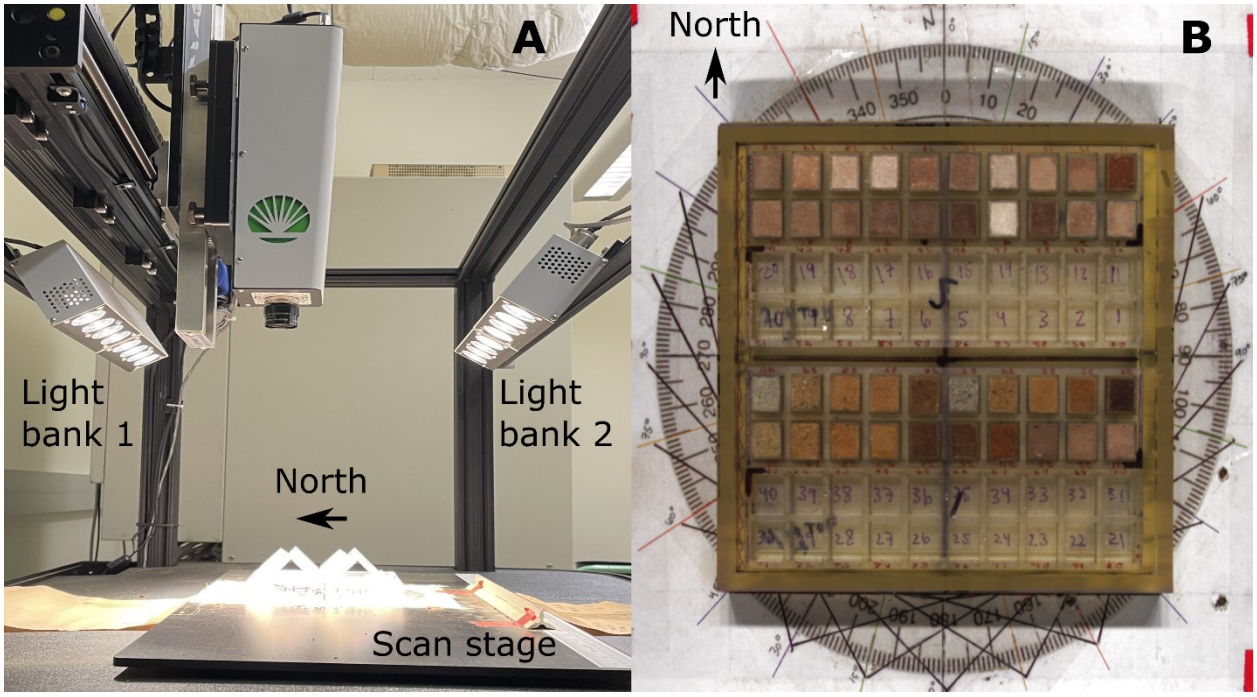

FIGURE 3: A) Photo of the hyperspectral imaging (HSI) setup showing the hyperspectral camera, both light banks, and the scan stage with the sample well array at the 50° slope and 0° aspect position. B) An example of a hyperspectral image (displaying only the red (674 nm), green (540 nm), and blue (437 nm) bands) of the sample well array containing prepared soil samples at a slope and aspect of 0°.

White calibration intensities for each waveband were obtained by collecting 100 spectra from each of the 862 pixels in the lateral spatial dimension (i.e., the number of linear pixels in the field of view of the camera) using a 30.5 x 30.5 cm Spectralon white reflectance panel (Labsphere, North Sutton, NH) prior to running each batch of samples. Dark calibration intensities were obtained in a similar manner as the white calibration intensities, except the lens cap was left on the hyperspectral camera and all the lights turned off.

2.5 HSI Data Processing

Each HSI scan generates a 3-D array with RI measured within two spatial dimensions (862 x ~862 pixels) and one spectral dimension of 471 VNIR wavebands. The resulting VNIR reflectance spectra were scaled between values of 0 (minimum RI) and 1 (maximum RI) using the measured dark and white calibration intensities, respectively (Equation 1):

$$RI_{cor} = \frac{RI_{obs} - \overline{RI}_{dark}}{\overline{RI}_{white} - \overline{RI}_{dark}} \quad (1)$$

where RI_{cor} is the RI of the dark and white corrected (or rescaled) sample spectra and RI_{obs} is the RI of the observed (or measured) sample spectra. The value of $\overline{RI}_{dark}$ was obtained by averaging the dark calibration intensities across the 100 spectra, 862 pixels in the lateral spatial dimension, and 471 wavebands. Thus, a single average $\overline{RI}_{dark}$ was subtracted from the RI of each waveband of the white calibration and sample spectra. White calibration intensities were averaged across the 100 spectra and 471 wavebands for each of the 862 lateral pixels separately to obtain $\overline{RI}_{white}$ to account for slight variation in illumination from the different bulbs in the light banks.

White and dark adjusted intensities for red (674 nm), green (540 nm), and blue (437 nm) wavebands were plotted for each pixel resulting in an RGB image (Figure 3b). This image was used to identify the row and column indices for automated extraction of each soil pixel within each sample well. Spectral signatures were isolated and spatially averaged across all extracted pixels within each sample well (i.e., typically ~680 pixels or 0.4 cm^2 for 0° aspect and 0° slope). This averaging resulted in a single reflectance spectrum for each of the 681 soil samples at each of the 91 unique slope and aspect configurations totaling to 61,971 reflectance spectra.

The automated procedure for isolating spectra from within sample wells resulted in extracting some spectra that were influenced by the sample well array. These spectra were identified with a combination of outlier detection and visual inspection and excluded as imaging errors. Briefly, spectra were removed from the analysis if they contained any RI values outside 1.5 times the interquartile range of all observed RI values or if they could be visually identified as errors using RBG images. Similarly, additional imaging errors were identified if differences between the non-zero slope spectra and zero-slope spectra were outside 1.5 times the interquartile range of all observed differences at each slope position.

The spectra for all 13 aspects measured at a slope of 0° were averaged into a single reference spectrum for each sample since we did not expect to see an aspect effect at 0° slope. This filtering and averaging approach reduced the total number of spectra analyzed in this study to 48,149 and the total number of unique non-reference slope and aspect configurations to 78. No further data reduction or transformation methods were implemented and all 471 data points for each reflectance spectrum were retained for analysis. All post-scan data processing and analysis were performed in R (R Core Team, 2022).

2.6 Topographic Corrections

We calculated a reference spectrum for each sample as the average RI of each waveband for all aspects scanned at a 0° slope to evaluate and correct for the change in RI caused by non-flat surface orientations. We compared four methods for correcting topographic influences on reflectance spectra at non-reference surface orientations: two empirical methods and two geometric-based approaches. These methods are referred to as the ΔI (empirical), ΔI+ (empirical), cosine (geometric), and C-corrections (geometric).

2.6.1 Empirical ΔI and ΔI+ Corrections

We calculated the difference between the reference spectrum for each sample and the uncorrected spectrum measured at each of the 78 non-reference slope and aspect configurations as follows:

$$\Delta I_{\lambda_i} = URI_{\lambda_i} - RRI_{\lambda_i} \quad (2)$$

where ΔI_{λ_i} is the difference between the uncorrected RI (URI) from a sample scanned in a non-reference orientation and the reference RI (RRI) for the ith waveband (λ_i). We refer to the resulting set of ΔI_{λ_i} values from Equation (2) for a single sample scanned at a particular slope and aspect configuration as a ΔI spectrum. These spectra indicate how much the RI increased (positive ΔI) or decreased (negative ΔI) relative to the RRI at each waveband.

We developed two multiple linear regression (MLR) models to predict the ΔI spectrum given the waveband (λ) and surface orientation (i.e., ϕ_o and η) of each sample. The first was of the form:

$$\Delta I_\lambda = \beta_0 + \beta_1\eta + \beta_2\phi_o + \beta_3\lambda \quad (3)$$

where β_0, β_1, β_2, and β_3 are regression coefficients in the model. The results of Equation (3) were used to correct each non-flat spectrum back to its corresponding reference spectrum using Equation (4):

$$RI_{\lambda_{\Delta I}} = URI_\lambda - \Delta I_\lambda \quad (4)$$

where $RI_{\lambda_{\Delta I}}$ is the RI that was corrected using the predicted ΔI_λ in Equation (3) and the URI_λ. We refer to this combination of Equation (3) and (4) as the ΔI correction approach.

The second MLR model developed included the interaction terms between slope, aspect, and waveband and was of the form:

$$\Delta I_\lambda = \beta_0 + \beta_1\eta + \beta_2\phi_o + \beta_3\lambda + \beta_4\eta\phi_o + \beta_5\eta\lambda + \beta_6\phi_o\lambda + \beta_7\eta\phi_o\lambda \quad (5)$$

where β_4, β_5, β_6, and β_7 are the regression coefficients associated with the additional interaction terms. We refer to the combination of Equations (4) and (5) as the ΔI+ correction method where $RI_{\lambda_{\Delta I+}}$ is the corrected RI using the predicted ΔI_λ in Equation (5) and URI_λ. Equations (3) and (5) were fit using ΔI spectra from each sample scanned at each non-reference orientation (i.e., N = 48,149). We also applied standardized MLR regression in this case to calculate β weights to examine the relative explanatory power of each variable.

2.6.2 Geometric Corrections

The first geometric correction—that is, the cosine correction— was implemented to remove the influence of surface topography on the VNIR spectra observed at non-reference orientations and results were compared to ΔI and ΔI+ corrections. This approach relies solely on the geometry of the lighting and hyperspectral camera setup as shown in Figures 3A and 4. The cosine-corrected spectrum ($RI_{\lambda_{cos}}$) for each non-reference orientation was obtained following Equation (6) (Teillet et al., 1982):

$$RI_{\lambda_{cos}} = URI_\lambda \frac{\overline{\cos\theta}}{\overline{\cos\gamma}} \quad (6)$$

where $\overline{\cos\theta}$ is the average of the cosine of the zenith angles (θ) between the hyperspectral camera and light bank 1 (θ_1) and 2 (θ_2). The $\overline{\cos\theta}$ term is calculated as:

$$\overline{\cos\theta} = \frac{\cos\theta_1 + \cos\theta_2}{2} \quad (7)$$

Similarly, the $\overline{\cos\gamma}$ in Equation (6) is the average of the cosine of the incident angles (γ) with respect to light bank 1 (γ_1) and 2 (γ_2) calculated as:

$$\overline{\cos\gamma} = \frac{\cos\gamma_1 + \cos\gamma_2}{2} \quad (8)$$

where cos γ is the illumination angle calculated from the slope, aspect, zenith, and azimuth (ϕ_a) angles for each light bank as (Civco, 1989):

$$\cos\gamma = \cos\theta\cos\eta + \sin\theta\sin\eta\cos(\phi_a - \phi_o) \quad (9)$$

Zenith angles were calculated directly from the HSI setup using:

$$\theta = \tan^{-1}\left(\frac{A}{E - H}\right) \quad (10)$$

where A is horizontal distance between each light bank and the hyperspectral camera, E is the height of the light bank above the scan stage, and H is the height of the sample surface above the scan stage (Figure 4 and Table S2). The azimuth angle for light bank 1 and 2 was 0° and 180°,

respectively (Figure 4). The slope and aspect angles were prescribed by the position of the soil sample within the sample array and under the hyperspectral camera (Figures 2-4).

The second geometric approach implemented was a wavelength-dependent variant of the cosine correction method termed the C-correction. The C-correction modifies the ratio between $\overline{\cos\theta}$ and $\overline{\cos\gamma}$ in Equation (6) with an empirically determined constant (C_λ) to calculate C-corrected spectrum (RI_C) following Equation (11):

$$RI_{\lambda_C} = URI_\lambda \frac{\overline{\cos\theta} + C_\lambda}{\overline{\cos\gamma} + C_\lambda} \tag{11}$$

The C_λ parameter was determined as:

$$C_\lambda = \frac{b_\lambda}{m_\lambda} \tag{12}$$

where b_λ and m_λ are the linear coefficients for the regression between $\overline{\cos\gamma}$ and URI_λ at each waveband (Teillet et al., 1982):

$$URI_\lambda = b_\lambda + m_\lambda \overline{\cos\gamma} \tag{13}$$

These empirical and geometric corrections were applied to all samples and orientations, and their performances were evaluated by comparing URI, $RI_{\Delta I}$, $RI_{\Delta I+}$, RI_{cos}, and RI_C to RRI to assess how well the uncorrected versus the corrected spectra at each orientation matched the reference spectrum for each soil sample.

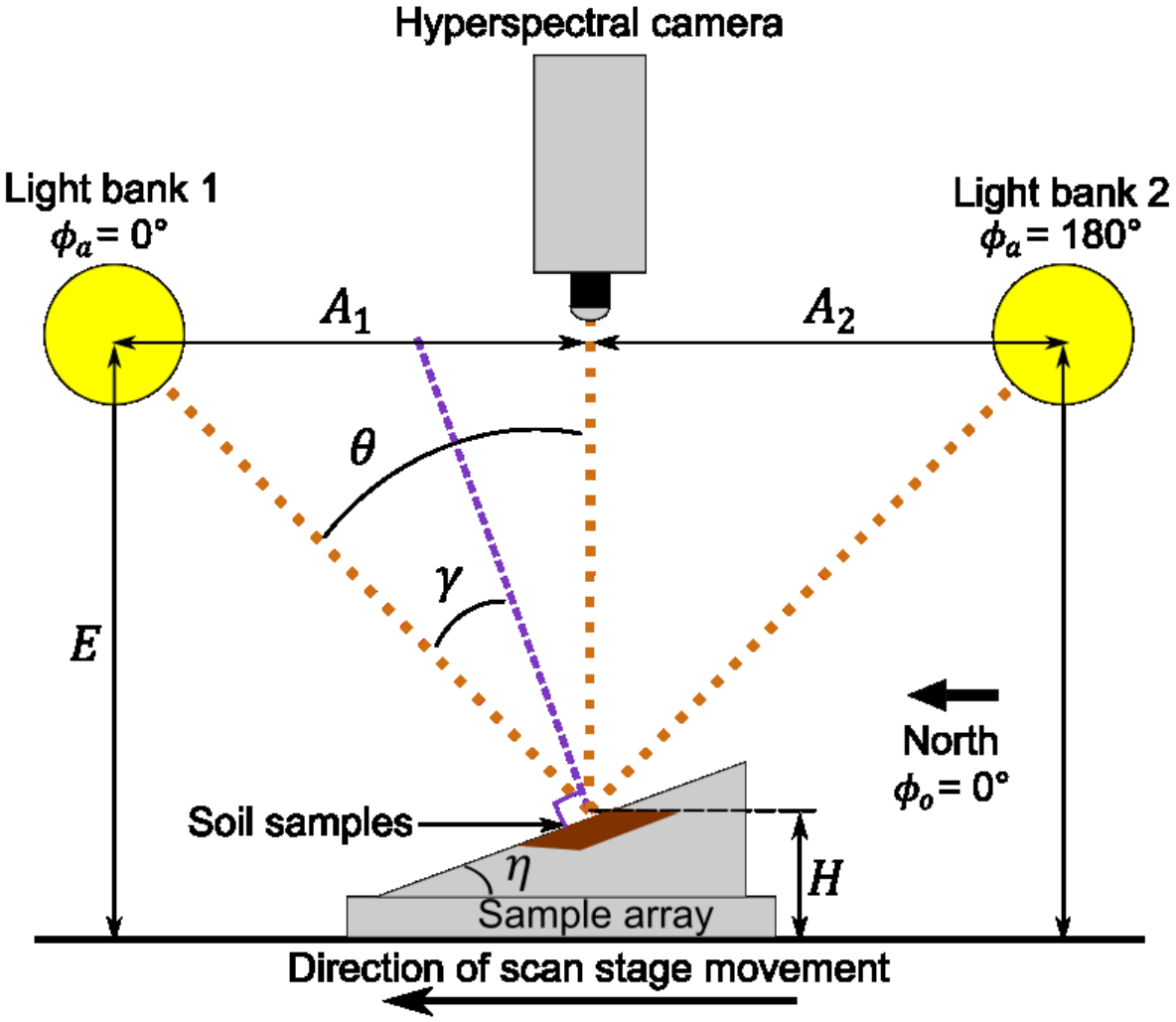

FIGURE 4: Diagram of the HSI setup including physical parameters used in geometric topographic corrections (also see Table S2).

2.7 SOC Prediction from Uncorrected and Corrected VNIR Reflectance Spectra

Two partial least squares regression (PLSR) models were trained and evaluated to predict SOC from VNIR soil reflectance spectra. The first model used the reference spectrum from each soil sample to train the model (N = 681), and thus ignored the role of surface topography in calibrating the PLSR model. We refer to this model as the reference PLSR model ($PLSR_{ref}$). The uncorrected spectra from each soil sample at each non-reference slope and aspect configurations were used to evaluate this PLSR model (N = 48,149 spectra). The observed SOC values were positively skewed and were log_{10} transformed before training both PLSR models (Minasny et al., 2011). The predicted log_{10}SOC (SOC_p) was then compared against observed

log_{10}SOC (SOC_o) to see how accurately the model predicted log_{10}SOC when the influence of surface topography on soil reflectance was ignored during model calibration and evaluation.

The second PLSR model was designed to reduce the impact of surface topography on SOC predictions by correcting the spectra prior to model calibration and evaluation. In this approach, the PLSR model training dataset contained one corrected spectrum per sample from a randomly chosen orientation (N = 681) and was referred to as the corrected PLSR model ($PLSR_{cor}$). These corrected spectra were calculated using the best performing topographic correction as described in section 2.8 below. This model was evaluated using corrected spectra from each soil sample at each non-reference surface orientation (N = 48,149 spectra). As with $PLSR_{ref}$, SOC_o and SOC_p were then compared to evaluate the performance of $PLSR_{cor}$ for predicting SOC from VNIR soil spectra and to assess whether our approach to accounting for surface topography improved SOC predictions.

2.8 Evaluating Topographic Corrections and SOC Model Performance

To evaluate the performance of the four topographic correction approaches, the root mean squared error (RMSE) was calculated between each corrected spectrum and the reference spectrum and compared to RMSE calculated between each uncorrected spectrum and reference spectrum (Equation 14). Similarly, to evaluate the accuracy of SOC predictions, RMSE was calculated between SOC_o and SOC_p obtained from calibration and evaluation of $PLSR_{ref}$ and $PLSR_{cor}$. The RMSE is used to assess how close URI, $RI_{\Delta I}$, $RI_{\Delta I+}$, RI_{cos}, or RI_C, is to RRI or how close SOC_p is to SOC_o. The RMSE was calculated as follows:

$$\mathrm{RMSE} = \sqrt{\frac{\sum_{i=1}^{N} (x_i - \hat{x}_i)^2}{N}} \tag{14}$$

where x_i is the ith observation of either RRI or SOC_o, $\hat{x}_i$ is the ith observation of either URI, $RI_{\Delta I}$, $RI_{\Delta I+}$, RI_{cos}, RI_C, or SOC_p, and N is the number of observations. The RMSE was used to determine which topographic correction performed best by comparing RMSE for each soil sample at each non-reference orientation across all wavelengths. The RMSE was calculated for each wavelength across all soil samples at each slope or aspect position to assess the performance of the topographic correction at each wavelength. An ideal RMSE of 0 indicates that the corrected or uncorrected RI perfectly matched the reference RI in the context of topographic correction performance evaluation or that SOC_p matches SOC_o in the context of PLSR model performance evaluation.

The Nash-Sutcliffe Efficiency (NSE) was also calculated to compare the performance of topographic correction approaches and SOC prediction models. The NSE is used to assess how much closer URI, $RI_{\Delta I}$, $RI_{\Delta I+}$, RI_{cos}, or RI_C, is to RRI than the mean of RRI or how much closer SOC_p is to SOC_o than the mean of SOC_o. The NSE was calculated as follows:

$$\mathrm{NSE} = 1 - \frac{\sum_{i=1}^{N} (x_i - \hat{x}_i)^2}{\sum_{i=1}^{N} (x_i - \bar{x})^2} \tag{15}$$

where x_i is the ith observation of either RRI or SOC_o, $\hat{x}_i$ is the ith observation of either URI, $RI_{\Delta I}$, $RI_{\Delta I+}$, RI_{cos}, RI_C, or SOC_p, $\bar{x}$ is the mean of all RRI or SOC_o, and N is the number of observations. The NSE was calculated for each soil sample at each orientation across all wavelengths in the context of topographic correction evaluation. An ideal NSE of 1 indicates that the uncorrected or corrected RI perfectly matches RRI, while an NSE of less than 0 indicates that the mean of RRI more closely matches RRI compared to the corrected RI. Similarly, in our evaluation of the PLSR models, an ideal NSE of 1 indicates that SOC_p perfectly matches SOC_o, while an NSE of less than 0 indicates that the mean of SOC_o was a better predictor than the PLSR model.

The α and β components of the Kling-Gupta efficiency (KGE) (Gupta et al., 2009) were compared to determine which method performed best in cases where the RMSE and NSE were similar for different topographic correction methods. The α component was computed as the ratio of the standard deviations (σ) of URI, $RI_{\Delta I}$, $RI_{\Delta I+}$, RI_{cos}, and RI_C to the standard deviation of RRI for each soil sample at orientation across all wavelengths using Equation (16) as follows:

$$\alpha = \frac{\sigma_{\hat{x}}}{\sigma_x} \tag{16}$$

where $\hat{x}$ is either URI, $RI_{\Delta I}$, $RI_{\Delta I+}$, RI_{cos}, and RI_C and x is RRI. The β component was computed as the ratio of the mean URI, $RI_{\Delta I}$, $RI_{\Delta I+}$, RI_{cos}, and RI_C to the mean of RRI for each soil sample at each orientation across all wavelengths using Equation (17) as follows:

$$\beta = \frac{\mu_{\hat{x}}}{\mu_x} \tag{17}$$

where $\hat{x}$ is either URI, $RI_{\Delta I}$, $RI_{\Delta I+}$, RI_{cos}, and RI_C and x is RRI. An ideal α of 1 indicates that the variability of uncorrected or corrected RI perfectly matches the variability of RRI, while an ideal β of 1 indicates that the mean RRI matches the mean corrected RI.

3 RESULTS AND DISCUSSION

3.1 Sample Characterization

Soil samples used for calibration of the empirical topographic corrections as well as the PLSR models used to predict SOC (N = 681) represent a wide range of soil properties (Table 1). The values of SOC captured by these samples ranged between 6.4E-4 and 0.17 g cm^{-3} with a mean of 0.028 (Table 1). Particle-size distributions fell within 11 of the 12 USDA textural classes excluding silt. Packed bulk density of soils within sample wells ranged between 0.57 to 2.0 g cm^{-3} with a mean of 1.6 and standard deviation of 0.2 (Table 1). The US Soil Taxonomy soil orders represented by these samples are Alfisols, Andisols, Aridisols, Inceptisols, Mollisols, Ultisols.

TABLE 1: Soil samples used in this study (N = 681) represent a wide range of soil organic carbon (SOC) and soil textures. Bulk density values represent the packed density in the sample well after samples were prepared for HSI scanning.

Property	Mean	Minimum	Maximum	Standard Deviation
SOC, g cm^{-3}	0.028	6.4E-4	0.17	0.028
SOC, wt. %	2.1	0.04	23	2.7
Sand, %	45	1.7	99	27.5
Silt, %	33	1.3	67	15.4
Clay, %	22	0	76	16.2
Packed bulk density, g cm^{-3}	1.6	0.57	2.0	0.20

3.2 Influence of Slope and Aspect on the VNIR Soil Reflectance Spectrum

The *URI* decreased compared to *RRI* with increases in slope, especially at NIR wavebands (Figure 5A). Barnes et al. (1989) observed a similar shift in near-infrared reflectance with changes in the slope of the sample presentation. The *URI* tended to decrease with increases in aspect within each slope position (Figure 5B), although the influence of aspect on the *URI* was not as clear as the influence of slope (Figures 6A and 6C). This can be seen from the RMSE and NSE results obtained by comparing *URI* to *RRI* which show that the distance between *URI* and *RRI* increases (i.e., RMSE increases and NSE decreases) more with increases in slope than with increases in aspect (Figure 6).

The mean and standard deviation of reflectance intensities observed across all soil samples and aspects at 0° slope for the 500 nm, 700 nm, and 900 nm wavelengths were calculated to assess whether an aspect effect was observed among spectra collected at 0° slope (i.e., among the spectra used to calculate *RRI*). These means were 0.16, 0.32, and 0.38, and their standard deviations were 0.0003, 0.0003, and 0.0004, respectively. These standard deviations indicate that reflectance spectra observed at the 0° slope position are unaffected by aspect.

The ratio of standardized regression squared β-weights obtained from calibration of the MLR model in the ΔI+ correction (see Comparison of Topographic Correction Methods section below) also shows that slope imparts a stronger influence than aspect on the difference between *URI* and *RRI* (Table 2). Therefore, slope imparts a stronger influence than aspect on the *URI* of soil samples.

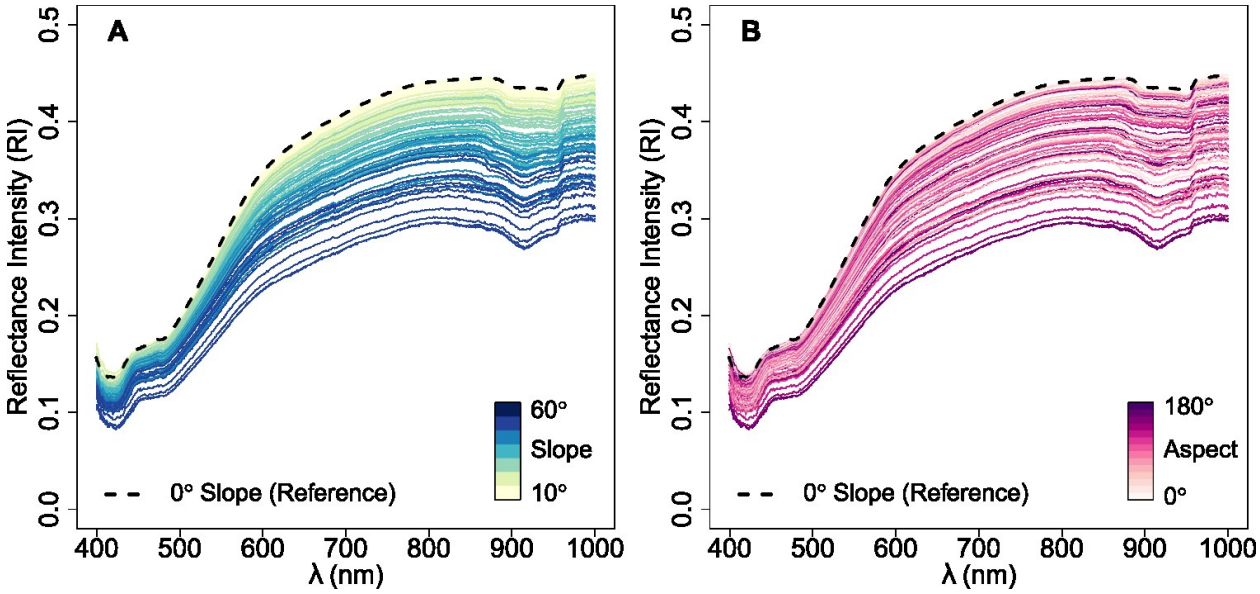

FIGURE 5: Uncorrected visible near-infrared (VNIR) soil spectra for a single representative soil sample at 78 slope (A) and aspect (B) configurations relative to the reference spectrum for this soil sample (black dashed). Slope exerts a stronger control on uncorrected reflectance intensity (URI) of soil samples compared to aspect.

3.3 Comparison of Topographic Correction Methods

Performance of four topographic correction methods were compared based on how well the topographically corrected spectra matched the reference spectrum. We compared RMSE and NSE of corrected versus reference spectra to that of uncorrected versus reference spectra to examine whether the influence of surface orientation on soil reflectance was reduced by implementing a topographic correction (Figure 6).

Overall, the RMSE of URI increased with increasing slope and aspect, and the magnitudes of errors were more pronounced with slope increases compared to aspect supporting our conclusion that slope imparts a stronger influence on soil reflectance than aspect (Figure 6). At the smallest slope angle (10°), the mean of RMSE values for the geometric and ΔI+ corrected spectra were similar to RMSE values for the uncorrected spectra, while the ΔI correction method resulted in the largest errors. At the 20° slope, the ΔI+ correction and the C-correction methods had the lowest errors, while the ΔI correction, and the cosine correction had similar errors to the uncorrected spectra. Hantson and Chuvieco (2011) also found that the cosine correction was the least successful of the topographic correction methods that they compared, which included the C-correction, particularly when cos γ is small. At 30°-60° slope angles, the cosine correction method had the largest errors which, as explained by Teillet et al. (1982), can be attributed to the overestimation of RI_{cos} due to small, even negative, cos γ at orientations where γ is large. This situation occurs, for example, from the perspective of light bank 2 when the soil sample surface is facing 0°N at high slope angles. Overall, the ΔI+ and C-

correction methods produced the smallest RMSE and NSE closest to 1 across all slope angles (Figure 6A and 6B).

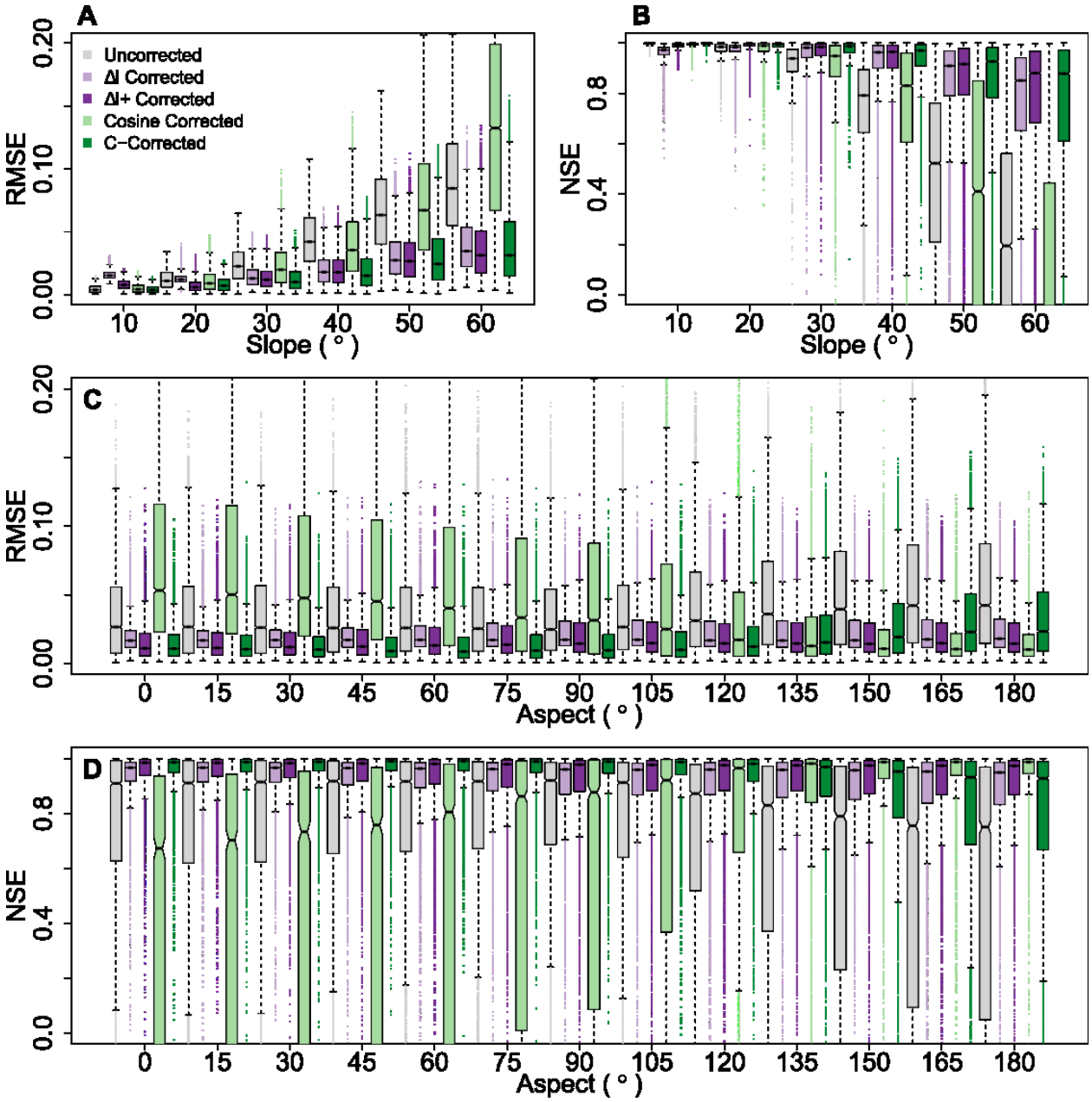

FIGURE 6: Root mean square error (RMSE) (A, C) and Nash-Sutcliffe Efficiency (NSE) (B, D) as functions of slope (A, B) and aspect (C, D) calculated across 471 wavebands for each soil spectrum (N = 48,149). The most successful correction method in terms of minimizing RMSE and maximizing NSE was the ΔI+ correction.

The RMSE and NSE of $RI_{\Delta I}$ and RI_C were similar at aspect angles less than 150°, while the RI_{cos} had the highest RMSE and lowest NSE, especially at aspect angles smaller than 135°. At aspects smaller than 135°, both empirical correction methods and the C-correction performed better than the cosine correction. The poorer performance of the cosine correction at 0°N aspect positions compared to 180°S aspect positions is because light bank 2 is farther away from the hyperspectral camera than the light bank 1 (Table S2). As a result, γ_2 from the perspective of light bank 2 when the sample is facing 0°N, is greater than γ_1 from the perspective of light bank 1 when the sample is facing 180°S causing a greater overestimation of RI_{cos} when ϕ_o is small and η is large compared to when ϕ_o is large (Teillet et al., 1982; Hantson and Chuvieco, 2011).

Since the C-correction method performance was close to that of the empirical corrections (i.e., no difference in mean RMSE and NSE), the α and β components of the KGE were compared across all slope and aspect angles (Figures S1 and S2). In addition to confirming that URI an RI_{cos} were farthest from the reference, these results showed that biases in the standard deviation of $RI_{\Delta I}$ deviated from unity at small and large aspect angles, while this pattern was not present in $RI_{\Delta I+}$ and RI_C (Figure S1). Also, biases in the mean and standard deviation of RI_C deviated from unity at small and large aspect angles, while this pattern was not present in $RI_{\Delta I+}$ (Figure S2). Therefore, comparison of these four topographic corrections showed that the empirical ΔI+ method provided the most consistent correction for the influence of surface topography on RI measured at non-flat surface orientations while being less complex than the non-linear geometric corrections.

We further illustrate the success of the ΔI+ correction by showing RMSE as a function of wavelength for uncorrected and ΔI+ corrected reflectance spectra across all soil samples grouped by either slope or aspect (Figure 7). These results confirm that the ΔI+ corrected spectra more closely match the reference spectrum than the uncorrected spectra across all wavebands, aspects, and all slopes except those at 10° (i.e., RMSE of ΔI+ corrected reflectance spectra are smaller than RMSE of uncorrected reflectance spectra).

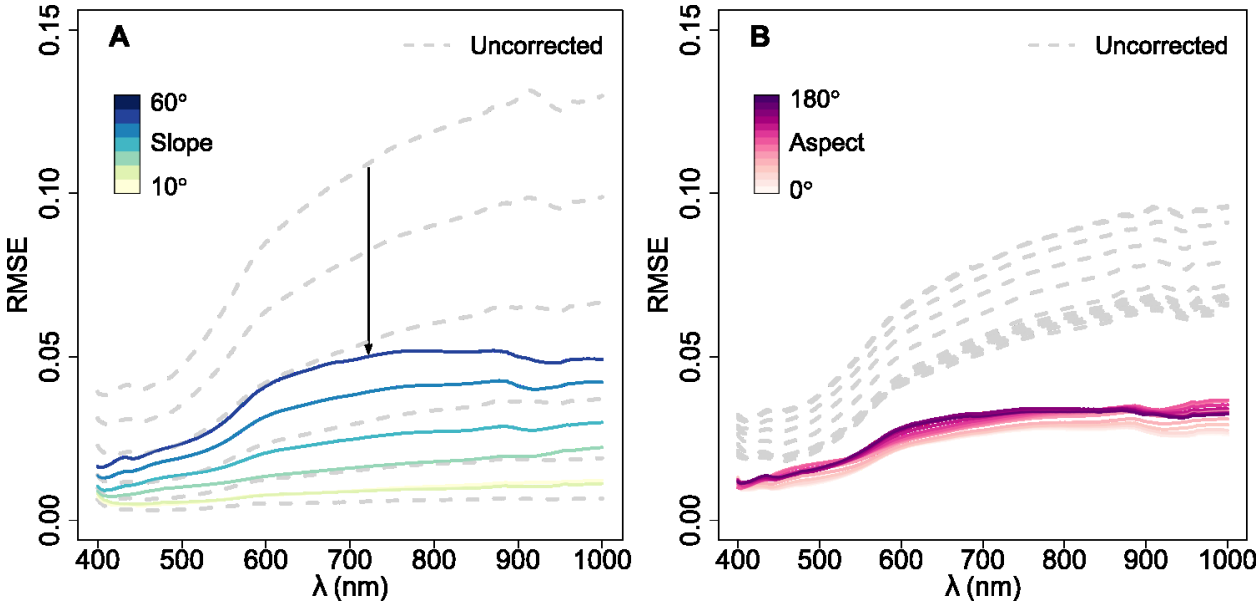

FIGURE 7: The RMSE as a function of wavelength calculated across all soil samples and across all aspect angles (A) or all slope angles (B) for uncorrected and the ΔI+ corrected spectra. The RMSE of uncorrected spectra are colored in grey while RMSE of ΔI+ corrected spectra are colored by slope (A) or aspect (B). The black arrow indicates how RMSE of the uncorrected spectra at the 60° slope corresponds to the RMSE of ΔI+ corrected spectra at the same slope. The ΔI+ corrected spectra more closely match the reference spectrum than the uncorrected spectra across all wavebands, aspects, and all slopes except those at 10°.

The empirically fitted coefficients of the MLR model used in the ΔI+ correction method and their β weights are provided to allow implementation of this method for similar HSI setups (Table 2). The ratio of standardized regression squared β-weights for slope and aspect is 15 indicating that slope explains about 15 times more variability in the difference between URI and RRI (i.e., ΔI) than aspect.

TABLE 2: Empirically fitted coefficients for the ΔI+ method as well as the standardized β weights for each predictor.

Parameter	β_0	β_1	β_2	β_3	β_4	β_5	β_6	β_7
Regression coefficient	-8.0E-3	6.4E-4	4.2E-6	3.8E-5	1.4E-7	-2.8E-6	4.2E-8	-6.7E-9
β weight	-0.0016	-0.65	-0.17	-0.32	-0.098	-0.23	-0.045	-0.025

The URI and $RI_{\Delta I+}$ for all 78 non-reference slope and aspect configurations of one representative soil sample and the corresponding RRI show that the corrected spectra resulting

from the ΔI+ method are closer to and more centered around the reference spectrum than the uncorrected spectra (Figure 8).

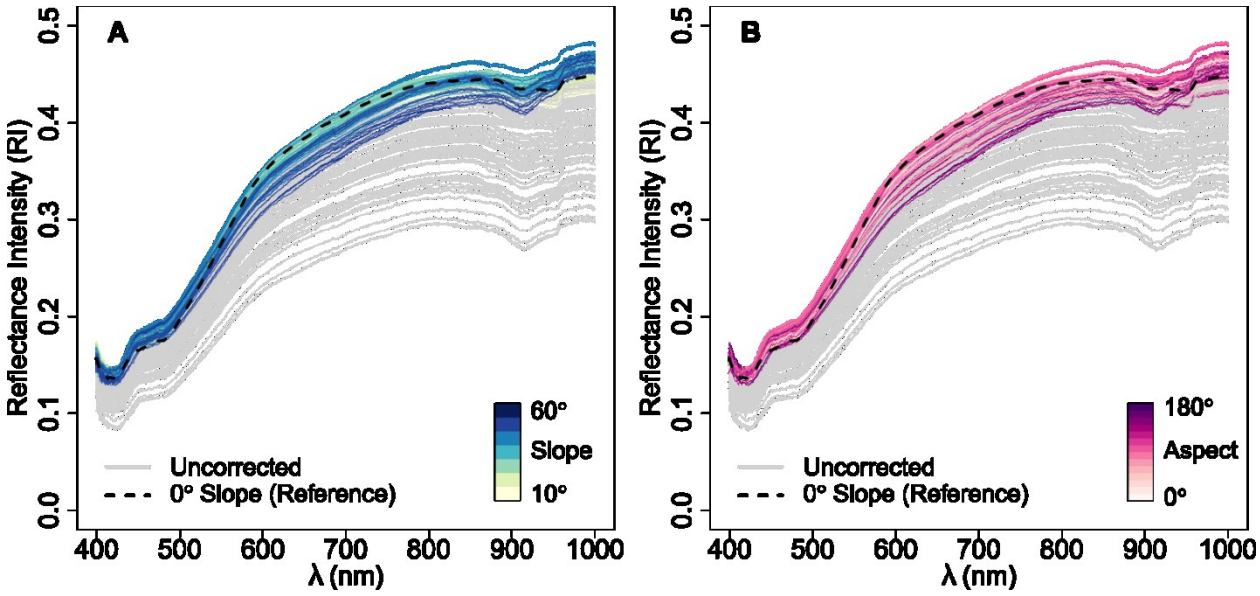

FIGURE 8: Uncorrected VNIR soil spectra from one representative soil sample at 78 non-reference surface orientations (grey) and the same 78 spectra after applying the ΔI+ topographic correction. Corrected spectra are colored by slope (A) or aspect (B) to show performance of the ΔI+ correction approach. Uncorrected spectra shown here in grey are the same as the uncorrected spectra colored by slope or aspect in Figure 5.

3.4 SOC Prediction from Uncorrected and Corrected VNIR Soil Reflectance Spectra

As described above, two approaches for SOC prediction using PLSR were implemented to assess whether reducing the impact of surface topography could improve SOC predictions made using VNIR soil reflectance spectra observed from non-flat surfaces. These results show that the $PLSR_{ref}$ model, which was trained on the reference spectra for each soil sample, performs better than the $PLSR_{cor}$ model, which was trained using ΔI+ corrected spectra from a single randomly chosen orientation for each soil sample (Figures 9A and 9C). This result is expected since the influence of surface topography is minimized when the soil sample is placed flat (i.e., 0° slope) under the hyperspectral camera, such as in the case of the reference spectra. When the $PLSR_{ref}$ model was evaluated using the uncorrected spectra, higher overall RMSE and bias in SOC_p was observed with increasing slope (i.e., the slopes of least squares regression lines fit at each slope position deviate from 1 with increasing slope position) (Figure 9B). This decrease in model performance was expected since non-flat surface orientation impacts RI (Baumgardner, 1985; Civco, 1989; Colby, 1991; Ben Dor et.al, 2015), and therefore the *URI* used for model evaluation are much different than the *RRI* used for model training.

As previously mentioned, when the $PLSR_{cor}$ model was trained and evaluated using ΔI+ corrected spectra from one randomly chosen orientation per sample, the RMSE is larger and R^2 is smaller than the reference model (Figure 9A and 9C). Poorer model performance is expected here as the influence of surface orientation has not been entirely removed from the ΔI+ corrected spectra whereas the influence of surface orientation on reference spectra is minimal. However, when the $PLSR_{cor}$ model is evaluated on ΔI+ corrected spectra from all 78 non-reference surface orientations, the increase in RMSE and decrease in R^2 (Figures 9C and 9D) are smaller than those seen when the $PLSR_{ref}$ model is evaluated using uncorrected spectra (Figures 9A and 9B). Also, the slopes of least squares regression lines between SOC_p and SOC_o at each slope position are closer to 1 indicating bias in SOC predictions is reduced when the $PLSR_{cor}$ model is evaluated using ΔI+ corrected spectra (Figure 9D) compared to when the $PLSR_{ref}$ model is evaluated using uncorrected spectra (Figure 9B). Larger R^2 and smaller RMSE and prediction bias across all slope positions confirm that implementing the ΔI+ topographic correction method in conjunction with training the PLSR model on the corrected spectra from a variety of sample surface orientations reduces the impact of non-flat surface orientation on SOC predictions.

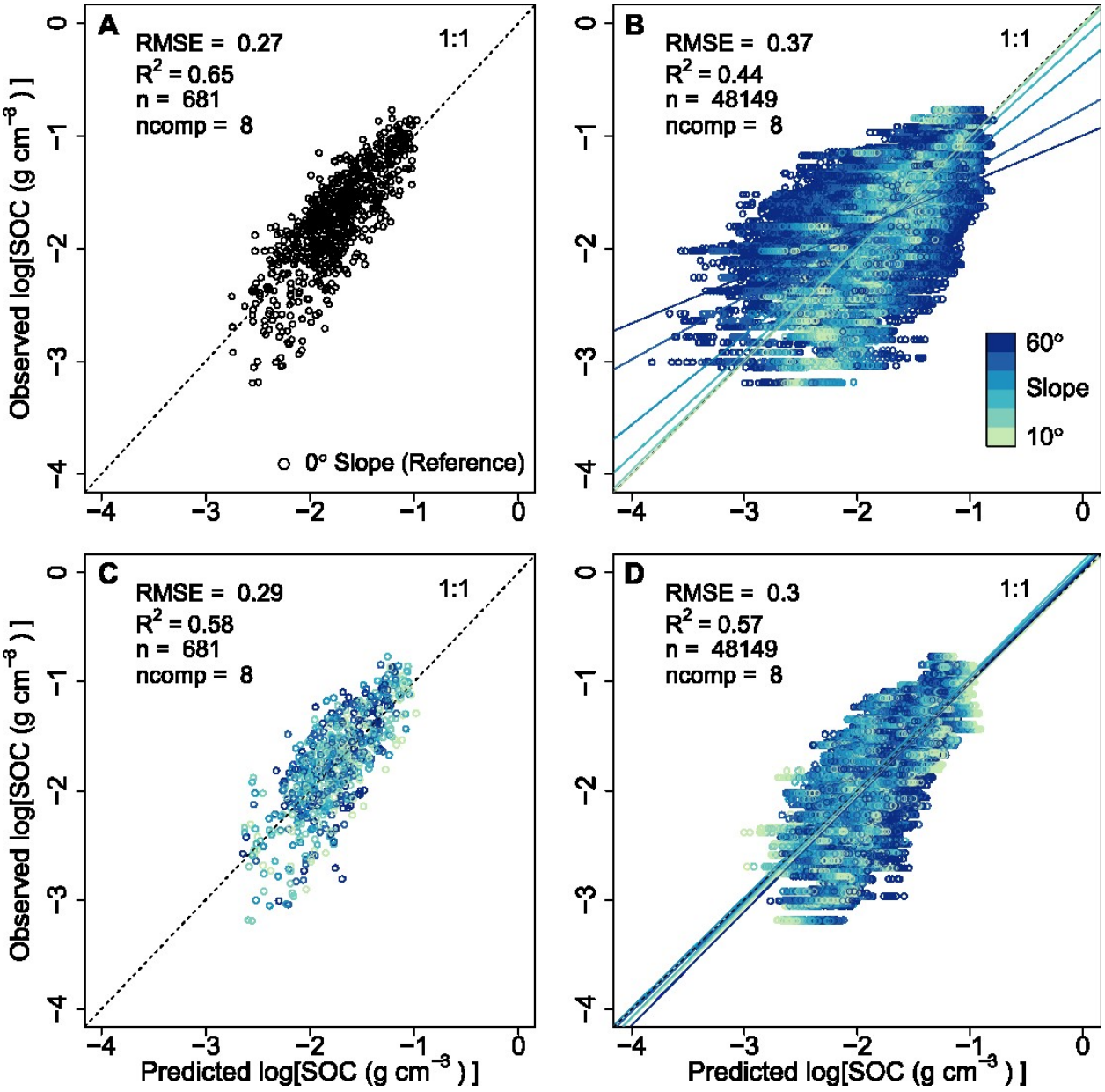

FIGURE 9: A) Performance of the PLSR model trained on the reference spectrum ($PLSR_{ref}$) at 0° slope for each soil sample (*N* = 681). B) Evaluation of $PLSR_{ref}$ using uncorrected spectra from all soil samples at all non-reference orientations (*N* = 48,149). C) Performance of PLSR model trained on corrected spectra from 1 randomly chosen orientation per sample ($PLSR_{cor}$) (*N* = 681). D) Evaluation of $PLSR_{cor}$ using ΔI+ corrected spectra from all soil samples at all non-reference orientations (*N* = 48,149). The best fit lines between observed and predicted SOC at each slope position are shown colored by slope in (B) and (D). Accounting for the influence of surface slope and aspect on VNIR reflectance spectra during training and evaluation of the PLSR model improved SOC predictions by decreasing bias and error and increasing R^2.

A comparison of RMSE and NSE values of SOC_o versus SOC_p resulting from evaluation of $PLSR_{ref}$ and $PLSR_{cor}$ models for each soil sample at each slope and aspect position show that RMSE is smaller and NSE is closer to 1 at all aspect angles and all except 10° and 20° slope angles for SOC predicted by the $PLSR_{cor}$ model compared to $PLSR_{ref}$ (Figure 10). These results indicate that SOC predictions are improved across all aspects and at slope angles greater than 30° when the influence of surface topography is considered. At 10° and 20° slopes, RMSE is closer to 0 and NSE is closer to 1 for SOC predictions made from uncorrected spectra using the $PLSR_{ref}$ model indicating that the $PLSR_{ref}$ model provided the best SOC predictions at these slope angles (Figure 10A and 10B). This observation is consistent with patterns observed in RMSE and NSE of uncorrected spectra when they are compared to the reference (Figure 6A and 6B). Therefore, a topographic correction might not be needed at small (e.g., 10°-30°) slope angles as the influence of surface orientation is minimal, however the importance of topographic correction becomes more pronounced as slope increases, particularly above 30°.

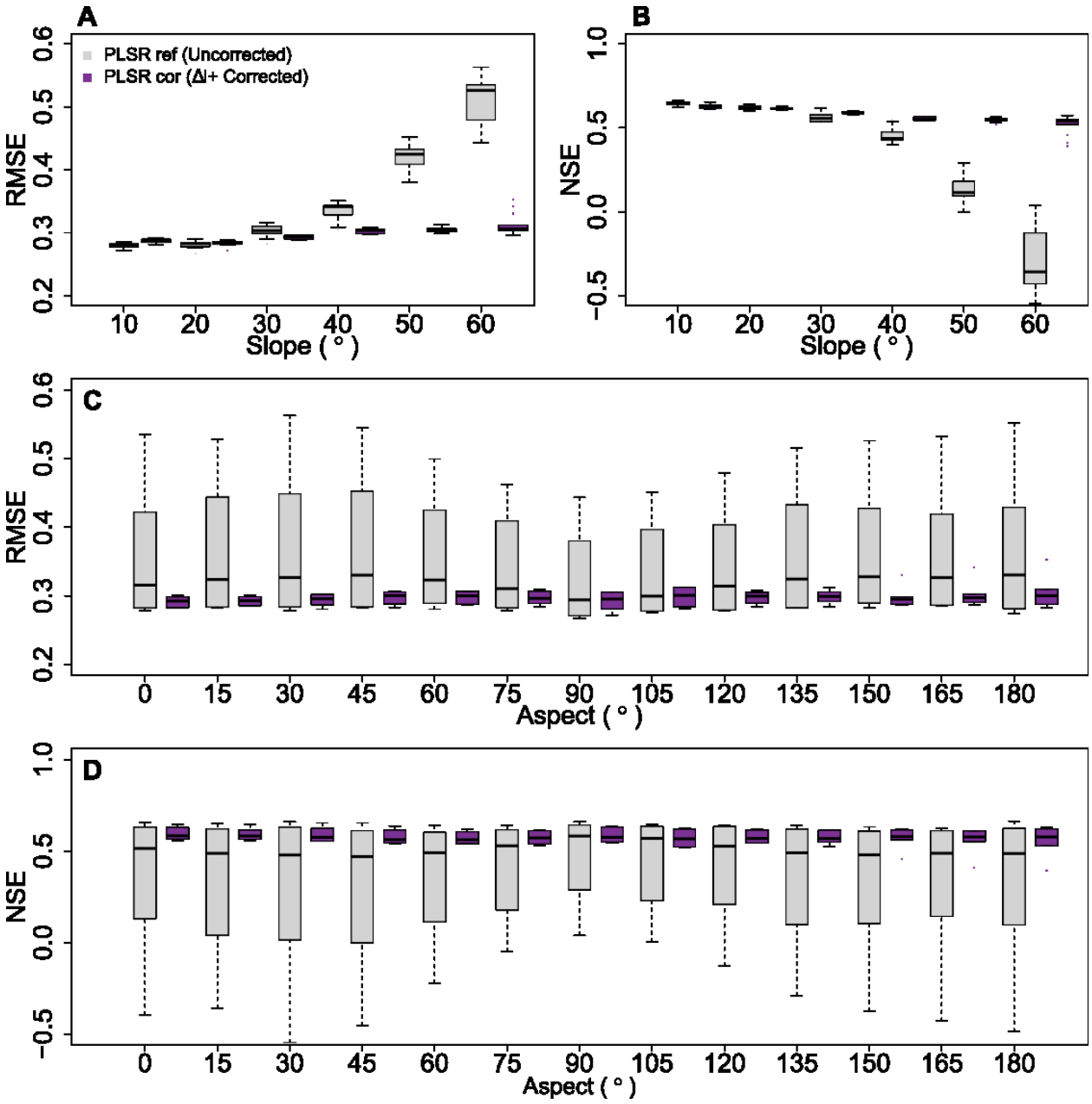

FIGURE 10: RMSE and NSE of predicted SOC for each soil sample at each slope (A, B) and aspect (C, D) angle show that SOC predictions are improved when the influence of surface topography is accounted for, particularly at slope angles greater than 30°.

4 CONCLUSION

This study showed that slope has a stronger influence on RI of soil samples compared to the aspect. We found that the ΔI+ empirical model based on slope, aspect, wavelength, and their interactions worked best for reducing the impact of surface orientation on soil reflectance and

improving SOC predictions made from soil reflectance spectra. Predicted SOC values were closer to laboratory measured SOC when the PLSR model was trained and evaluated on corrected VNIR soil reflectance spectra using the ΔI+ correction approach across all aspect angles and slope angles greater than 30°. This is likely because the influence of surface geometry on soil reflectance was least apparent at low slope angles and indicates that a topographic correction may not be necessary at slope angles smaller than 30°.

The calibration soil samples included here cover a wide range of soil properties including soil color, texture, and SOC, such that the ΔI+ correction equation could be applied to correct VNIR soil reflectance spectra for similar laboratory-based HSI setups. This study also provides a framework for topographic correction of spectra that could be applied to systems with different setup geometries.

Soil properties such as particle size that influence soil reflectance spectra (Barnes et al., 1989; Soriano-Disla et al., 2014) could also impact the difference in URI and RRI (i.e., ΔI). Therefore, including soil properties in addition to slope, aspect, and wavelength as ΔI_{λ_i} predictor variables in the MLR model used in the ΔI+ correction approach might improve empirical corrections. However, we did not explore the effect of soil properties on ΔI_{λ_i} since this correction is designed to adjust reflectance spectra of non-flat intact soil samples where these properties would not be available for each pixel. Additionally, the quality of SOC predictions made using reflectance spectra obtained from ground (pulverized) versus unground samples can vary with the area of soil being scanned (i.e., pixel size) (Reeves et al., 2002). Therefore, the effect of soil texture on reflectance spectra and thus predictions of ΔI_{λ_i} might also vary with pixel size. These relationships were beyond the scope of this study but should be investigated in the future to apply this method to pixels which are smaller (~250 x 250 μm) than the pixel size of sample wells (~0.7 x 0.9 cm) used to calibrate the ΔI+ correction equation and PLSR model developed here.

This novel empirical topographic correction approach has the potential to advance our ability to use VNIR HSI spectroscopy for mapping soil chemical structure on horizon-scale intact monoliths with rough surfaces, such as those prepared for soil structure characterization. This method clears the way for coupling HSI with other proximal sensing methods such as MLT scanning to simultaneously quantify soil physical and chemical structure on intact samples (Hirmas et al., 2016). In addition to soil structure characterization, MLT scanning provides vector normal values for each pixel which can be used to determine the surface geometry information needed for the topographic correction approach presented here. However, other proximal sensing techniques such as structure-from-motion photogrammetry could also provide this information. Simultaneously mapping soil structure along with soil chemical properties like SOC at fine (e.g., sub-mm) resolution at the horizon scale will likely provide data necessary for studies investigating the location of SOC and its relationship to soil aggregation and pore networks and, therefore, advance our understanding of water and carbon fluxes within soils.

SUPPLEMENTAL MATERIAL

The supplemental material contained in Tables S1 and S2 includes additional details about the geometry of the HSI spectrometer and soil samples used in this study which support future application of this method. Figures S1 and S2 support the conclusions drawn from Figure 6 and show that the ΔI+ correction method outperforms the ΔI, cosine, and C-correction methods.

REFERENCES

Bagnall, D.K., Jones, E.J., Balke S., Morgan, C.L.S., & McBratney, A.B. (2020). An in situ method for quantifying tillage effects on soil structure using multistripe laser triangulation. *Geoderma, 380*, 114642. https://doi.org/10.1016/j.geoderma.2020.114642

Banwart, S., Black, H., Cai, Z., Gicheru, P., Joosten, H., Victoria, R., Milne, E., Noellemeyer, E., Pascual, U., Nziguheba, G., Vargas, R., Bationo, A., Buschiazzo, D., de-Brogniez, D., Melillo, J., Richter, D., Termansen, M., Van Noordwijk, M., Goverse, T., … Montanarella, L. (2014). Benefits of soil carbon: Report on the outcomes of an international scientific committee on problems of the environment rapid assessment workshop. *Carbon Management, 5*(2), 185–192. https://doi.org/10.1080/17583004.2014.913380

Barnes, R. J., Dhanoa, M. S., & Lister, S. J. (1989). Standard normal variate transformation and de-trending of near-infrared diffuse reflectance spectra. *Applied Spectroscopy, 43*(5), 772–777. https://doi.org/10.1366/0003702894202201

Basile-Doelsch, I., Balesdent, J., & Pellerin, S. (2020). Reviews and syntheses: The mechanisms underlying carbon storage in soil. *Biogeosciences, 17*(21), 5223–5242. https://doi.org/10.5194/bg-17-5223-2020

Baumgardner, M. F., Silva, L. F., Biehl, L. L., & Stoner, E. (1985). Reflectance Properties of Soils. *Advances in Agronomy. 38*. 1-44. https://doi.org/10.1016/S0065-2113(08)60672-0

Ben Dor, E., Ong, C., & Lau, I. C. (2015). Reflectance measurements of soils in the laboratory: Standards and protocols. *Geoderma, 245–246*, 112–124. https://doi.org/10.1016/j.geoderma.2015.01.002

Bronick, C. J., & Lal, R. (2005). Soil structure and management: A review. *Geoderma, 124*(1–22). https://doi.org/10.1016/j.geoderma.2004.03.005

Browning, D., &. Stanish, L. (2017). Guidelines for the NEON soil characterization effort.

Buddenbaum, H., & Steffens, M. (2012a). Mapping the distribution of chemical properties in soil profiles using laboratory imaging spectroscopy, SVM and PLS regression. *EARSeL eProceedings*, *11*, 25-32.

Buddenbaum, H., & Steffens M. (2012b). The effects of spectral pretreatments on chemometric analyses of soil profiles using laboratory imaging spectroscopy. *Applied and Environmental Soil Science, 2012*, 274903. https://doi.org/10.1155/2012/274903

Civco, D. L. (1989). Topographic normalization of Landsat thematic mapper digital dmagery. *Photogrammetric Engineering and Remote Sensing, 55*(9), 1303-1309.

Davidson, E. A., & Janssens, I. A. (2006). Temperature sensitivity of soil carbon decomposition and feedbacks to climate change. *Nature, 440*, 165–173. https://doi.org/10.1038/nature04514

Eck, D. V., Hirmas, D. R., & Giménez, D. (2013). Quantifying soil structure from field excavation walls using multistripe laser triangulation scanning. *Soil Science Society of America Journal, 77*(4), 1319–1328. https://doi.org/10.2136/sssaj2012.0421

Gupta, H. V., Kling, H., Yilmaz, K. K., & Martinez, G. F. (2009). Decomposition of the mean squared error and NSE performance criteria: Implications for improving hydrological modelling. *Journal of Hydrology, 377*(1–2), 80–91. https://doi.org/10.1016/j.jhydrol.2009.08.003

Hantson, S., & Chuvieco, E. (2011). Evaluation of different topographic correction methods for Landsat imagery. *International Journal of Applied Earth Observation and Geoinformation, 13*(5), 691–700. https://doi.org/10.1016/j.jag.2011.05.001

Hirmas, D. R. (2013). A simple method for removing artifacts from moist fine-textured soil faces. *Soil Science Society of America Journal, 77*(2), 591–593. https://doi.org/10.2136/sssaj2012.0418n

Hirmas, D.R., Gimenez D., Mome Filho E.A., Patterson M., Drager K., Platt B.F., and Eck D.V. (2016). Quantifying soil structure and porosity using three-dimensional laser scanning. In Hartemink, A.E. and Minasny, B. (Eds.), *Digital Soil Morphometrics* (pp. 19-35). Springer, Switzerland. https://doi.org/10.1007/978-3-319-28295-4_2

Hirmas, D.R., Steffens, M., Sullivan, P., Zhang, C., & Giménez, D. (2016). Coupling multistripe laser triangulation with hyperspectral imaging VisNIR spectroscopy to elucidate the feedbacks between soil structure, hydrology, and organic matter. *18*, 10651.

Hirmas, D. R., Giménez, D., Nemes, A., Kerry, R., Brunsell, N. A., & Wilson, C. J. (2018). Climate-induced changes in continental-scale soil macroporosity may intensify water cycle. *Nature, 561*, 100–103. https://doi.org/10.1038/s41586-018-0463-x

Hobley, E., Steffens, M., Bauke, S. L., & Kögel-Knabner, I. (2018). Hotspots of soil organic carbon storage revealed by laboratory hyperspectral imaging. *Scientific Reports, 8*, 13900. https://doi.org/10.1038/s41598-018-31776-wLal, R. (2004). Soil carbon sequestration impacts on global climate change and food security. *Science, 304*(5677), 1623–1627. https://doi.org/10.1126/science.1097396

Lehmann, J., & Kleber, M. (2015). The contentious nature of soil organic matter. *Nature, 528*, 60–68. https://doi.org/10.1038/nature16069

Letey, J. (1991). The study of soil structure—Science or art. *Soil Research, 29*(6), 699. https://doi.org/10.1071/SR9910699

Lucas M., Pihlap E., Steffens M., Vetterlein D., & Kögel-Knabner I. (2020). Combination of imaging infrared spectroscopy and x-ray computed microtomography for the investigation of bio and physicochemical processes in structured soils. *Frontiers in Environmental Science*, *8*, 1-12. https://doi.org/10.3389/fenvs.2020.00042

McBratney, A.B., Stockmann, U., Angers, D.A., Minasny, B., Field, D.J. (2014). Challenges for soil organic carbon research. In Hartemink, A.E. and Minasny, B. (Eds.), Soil Carbon. *Progress in Soil Science*, (pp. 3-16). Springer, Switzerland. https://doi.org/10.1007/978-3-319-04084-4_1

Minasny, B., McBratney, A.B., Bellon-Maurel, V., Roger, J.-M., Gobrecht, A., Ferrand, L., & Joalland, S. (2011). Removing the effect of soil moisture from NIR diffuse reflectance spectra for the prediction of soil organic carbon. *Geoderma, 167–168*, 118–124. https://doi.org/10.1016/j.geoderma.2011.09.008

Or, D., Keller, T., & Schlesinger, W. H. (2021). Natural and managed soil structure: On the fragile scaffolding for soil functioning. *Soil and Tillage Research, 208*. https://doi.org/10.1016/j.still.2020.104912

Rabot, E., Wiesmeier, M., Schlüter, S., & Vogel, H.-J. (2018). Soil structure as an indicator of soil functions: A review. *Geoderma, 314,* 122–137. https://doi.org/10.1016/j.geoderma.2017.11.009

Reeves, J., McCarty, G., & Mimmo, T. (2002). The potential of diffuse reflectance spectroscopy for the determination of carbon inventories in soils. *Environmental Pollution, 116*(1), S277–S284. https://doi.org/10.1016/S0269-7491(01)00259-7

Schoeneberger, P.J., Wysocki D.A., Benham E.C., & Soil Survey Staff. (2012). *Field book for describing and sampling soils, Version 3.0.* Natural Resources Conservation Service, National Soil Survey Center, Lincoln, NE.

Six, J., Bossuyt, H., Degryze, S., & Denef, K. (2004). A history of research on the link between (micro)aggregates, soil biota, and soil organic matter dynamics. *Soil and Tillage Research, 79*(1), 7–31. https://doi.org/10.1016/j.still.2004.03.008

Soil Survey Staff. (2022). *Kellogg Soil Survey Laboratory methods manual. Soil Survey Investigations Report No. 42, Version 6.0.* U.S. Department of Agriculture, Natural Resources Conservation Service.

Soil Survey Staff. (2023). Web soil survey. Natural Resources Conservation Service, United States Department of Agriculture. Available online at the following link: http://websoilsurvey.sc.egov.usda.gov/. Accessed [6/6/2023].

Soriano-Disla, J. M., Janik, L. J., Viscarra Rossel, R. A., Macdonald, L. M., & McLaughlin, M. J. (2014). The performance of visible, near-, and mid-infrared reflectance spectroscopy for prediction of soil physical, chemical, and biological properties. *Applied Spectroscopy Reviews, 49*(2), 139–186. https://doi.org/10.1080/05704928.2013.811081

Steffens, M., & Buddenbaum, H. (2013). Laboratory imaging spectroscopy of a stagnic Luvisol profile—High resolution soil characterisation, classification and mapping of elemental concentrations. *Geoderma, 195–196*, 122–132. https://doi.org/10.1016/j.geoderma.2012.11.011

Steffens, M., Kohlpaintner, M., & Buddenbaum, H. (2014). Fine spatial resolution mapping of soil organic matter quality in a Histosol profile: Fine spatial resolution mapping of soil organic matter quality. *European Journal of Soil Science, 65*(6), 827–839. https://doi.org/10.1111/ejss.12182

Steffens, M., Zeh, L., Rogge, D. M., & Buddenbaum, H. (2021). Quantitative mapping and spectroscopic characterization of particulate organic matter fractions in soil profiles with imaging VisNIR spectroscopy. *Scientific Reports, 11*. https://doi.org/10.1038/s41598-021-95298-8

Stockmann, U., Adams, M. A., Crawford, J. W., Field, D. J., Henakaarchchi, N., Jenkins, M., Minasny, B., McBratney, A. B., Courcelles, V. D. R. D., Singh, K., Wheeler, I., Abbott, L., Angers, D. A., Baldock, J., Bird, M., Brookes, P. C., Chenu, C., Jastrow, J. D., Lal, R., … Zimmermann, M. (2013). The knowns, known unknowns and unknowns of sequestration of soil organic carbon. *Agriculture, Ecosystems & Environment, 164*, 80–99. https://doi.org/10.1016/j.agee.2012.10.001

Sullivan, P. L., Billings, S. A., Hirmas, D., Li, L., Zhang, X., Ziegler, S., Murenbeeld, K., Ajami, H., Guthrie, A., Singha, K., Giménez, D., Duro, A., Moreno, V., Flores, A., Cueva, A., Koop, Aronson, E. L., Barnard, H. R., Banwart, S. A., … Wen, H. (2022). Embracing the dynamic nature of soil structure: A paradigm illuminating the role of life in critical zones of the Anthropocene. *Earth-Science Reviews, 225*. https://doi.org/10.1016/j.earscirev.2021.103873

Teillet, P. M., Guindon, B., & Goodenough, D. G. (1982). On the slope-aspect correction of multispectral scanner data. *Canadian Journal of Remote Sensing, 8*(2), 84–106. https://doi.org/10.1080/07038992.1982.10855028

Vogel, H., Balseiro-Romero, M., Kravchenko, A., Otten, W., Pot, V., Schlüter, S., Weller, U., & Baveye, P. C. (2022). A holistic perspective on soil architecture is needed as a key to soil functions. *European Journal of Soil Science, 73*(1). https://doi.org/10.1111/ejss.13152

Wiesmeier, M., Urbanski, L., Hobley, E., Lang, B., von Lützow, M., Marin-Spiotta, E., van Wesemael, B., Rabot, E., Ließ, M., Garcia-Franco, N., Wollschläger, U., Vogel, H.-J., & Kögel-Knabner, I. (2019). Soil organic carbon storage as a key function of soils—A review of drivers and indicators at various scales. *Geoderma, 333*, 149–162. https://doi.org/10.1016/j.geoderma.2018.07.026